

Extreme Weather Variability on Hot Rocky Exoplanet 55 Cancri e Explained by Magma Temperature-Cloud Feedback

KAITLYN LOFTUS ^{1,*} YANGCHENG LUO ^{2,*} BOWEN FAN ³ AND EDWIN S. KITE ³

¹*Climate School, Columbia University, New York, NY 10025, USA*

²*Laboratoire de Météorologie Dynamique/Institut Pierre-Simon Laplace, Sorbonne Université, École Normale Supérieure, Université Paris Sciences et Lettres, École Polytechnique, Institut Polytechnique de Paris, Centre National de la Recherche Scientifique, Paris 75005, France*

³*Department of the Geophysical Sciences, The University of Chicago, Chicago, IL 60637, USA*

ABSTRACT

Observations of the ultra-short period rocky exoplanet 55 Cancri e (55 Cnc e) indicate that the planet's dayside infrared radiation fluctuates by a factor of at least six on sub-weekly timescales, for unknown reasons. We propose a feedback mechanism where increased reflective clouds cool surface magma, subsequently reducing cloud formation, which may offer a potential explanation for these phenomena. In this mechanism, under less cloudy conditions, stellar radiation heats the surface magma, causing it to release more silicate vapor, which then condenses to form reflective clouds. Once formed, these clouds reduce stellar insolation at the surface, leading to surface cooling, which in turn reduces vapor supply, decreasing cloudiness. A time lag between the temperature increase of surface magma and the subsequent increase in cloudiness—likely due to lagged atmospheric transport of cloud-forming vapor—enables self-sustained oscillations in surface temperature and cloud reflectivity. These oscillations manifest as variations in both the emitted thermal radiation and the reflected stellar radiation, causing variability in secondary eclipse depths across different wavelengths without significantly affecting the transit depth. Using a simple model, we find that diverse planetary parameters can reproduce the observations. Additionally, we demonstrate that secondary eclipse depths at different wavelengths can oscillate out of phase, consistent with recent observations by the James Webb Space Telescope. Finally, we discuss observational strategies to test this proposed mechanism on 55 Cancri e. If confirmed, observable ocean-atmosphere dynamics on exoplanets would open a new window into the composition, evolution, and fate of rocky planet volatiles.

Keywords: Exoplanets (498) — Exoplanet atmospheres (487) — Extrasolar rocky planets (511) — Planetary atmospheres (1244) — Atmospheric Clouds (2180)

1. INTRODUCTION

The super-Earth 55 Cancri e is an extraordinary target for exoplanet observation and planetary geoscience. The planet orbits a G-type star at an exceptionally short distance (Winn et al. 2011; Demory et al. 2011), which heats 55 Cancri e to extreme temperatures, making its 3×10^{21} W thermal emission distinguishable from that of the host star. Its short orbital period (<18 hours) allows for multiple measurements of the planet's thermal emission flux through secondary eclipse photometry or spectroscopy using space telescopes, such as Spitzer and the James Webb Space Telescope (JWST) (Demory et al. 2012, 2016a,b; Tamburo et al. 2018; Mercier et al. 2022; Hu et al. 2024; Patel et al. 2024). Recent JWST observations of this super-Earth, using secondary eclipse spectroscopy, have suggested the presence of an atmosphere rich in CO₂ or CO (Hu et al. 2024). If confirmed, this would mark the first detection of an atmosphere surrounding a rocky exoplanet.

Corresponding author: Yangcheng Luo
yangcheng.luo@lmd.ipsl.fr

* These authors contributed equally.

A notable puzzle revealed by these observations is the temporal variability of the thermal emission flux from the planet, of unknown cause. This variability “[implies] that it undergoes a global energy balance change more than 10,000 times greater than that from anthropogenic climate change on Earth” (Kite et al. 2021). In the Spitzer IRAC 4.5 μm channel, Demory et al. (2016a) reported that the secondary eclipse depth varied between 47 parts-per-million (ppm) and 176 ppm over eight occultations within two years, corresponding to a dayside 4.5 μm brightness temperature varying between ~ 1300 K and ~ 2800 K. Subsequent reanalysis by Tamburo et al. (2018) corroborated this variability. Recent analysis of JWST/NIRCam observations reported secondary eclipse depths in the 4.5 μm band that rapidly varied from 7 ppm to 119 ppm within one week (Patel et al. 2024).

In addition to the variability in the mid-infrared (mid-IR), varying secondary eclipse depths across visible to near-IR bands have also been observed (Meier Valdés et al. 2022; Demory et al. 2023; Patel et al. 2024). TESS observations in the 600–1000 nm bandpass show secondary eclipse depths varying between zero and 15 ppm over two years (Meier Valdés et al. 2022), CHEOPS observations in the 400–1000 nm bandpass show variations between zero and 166 ppm over two years (Demory et al. 2023), and JWST/NIRCam observations report variations between zero and 47 ppm at 2.1 μm (Patel et al. 2024). Both reflected starlight and the planet’s thermal emission can contribute to secondary eclipse depths in the visible and near-IR bands, so this visible and near-IR variability could indicate changes in both sources. The observed close-to-zero secondary eclipse depths in these bands suggest that the planet at times has a very low albedo. In contrast, observations of transit depths have not yet provided conclusive evidence of temporal variability (Demory et al. 2016a; Tamburo et al. 2018; Meier Valdés et al. 2022).

Several physical mechanisms have been proposed to explain the observed variability in secondary eclipse depths, including variability in the stellar flux induced by stochastically appearing star spots (Tamburo et al. 2018), magnetic star-planet interaction (Bourrier et al. 2018a; Folsom et al. 2020), catastrophic planetary disintegration (Meier Valdés et al. 2022), an inhomogeneous dust torus around the planet (Meier Valdés et al. 2023), asynchronous rotation of the planet with a hot spot on its surface (Tamburo et al. 2018), volcanic plumes temporarily elevating the altitude of the planetary photosphere (Demory et al. 2016a), and an imbalance between stochastic outgassing and atmospheric escape leading to transient atmospheres (Heng 2023). Among these mechanisms, variability in the stellar flux is considered unlikely (Tamburo et al. 2018) as the host star is quiet (Fischer et al. 2008). Star-planet interaction has been ruled out because the energy associated with magnetic star-planet interaction is orders of magnitude smaller than that required to induce the observed variations (Morris et al. 2021). Planetary disintegration is disfavored because an asymmetric transit shape indicative of a tail of a disintegrating planet has not been observed (Meier Valdés et al. 2022). The hypothesis of a dust torus has difficulty explaining the relatively constant transit depths (Heng 2023). Recent JWST observations have found that the variability in the secondary eclipse depths in two bandpasses is not correlated and thus do not support the hypothesis of a 3:2 spin-orbit resonance as the explanation (Patel et al. 2024). For the hypothesis involving transient atmospheres caused by stochastic outgassing (Heng 2023, see also Heng 2024), it is challenging for both atmospheric escape and outgassing rates to be sufficiently high to account for the variability (timescales of a week or less are reported by Patel et al. 2024).

This study proposes an alternative mechanism involving reflective silicate clouds and their self-regulating effect on their own formation rate (e.g., Rappaport et al. 2012) to explain the observed variability in secondary eclipse depths. We suggest that reflective clouds, formed from silicate vapor evaporated from a magma ocean, can attenuate stellar radiation reaching the surface, leading to surface cooling and a slowdown of the evaporation of silicates, thereby suppressing further cloud formation. This feedback, coupled with a delayed response of cloudiness to surface temperature change due to various possible processes, could result in self-sustained oscillations in the planet’s thermal emission flux and reflected starlight.

This study builds on previous modeling works on 55 Cancri e, which suggested that clouds composed of refractory materials, such as magnesium silicates and silicon oxides, could form and even exhibit high opacity (Mahapatra et al. 2017; Hammond & Pierrehumbert 2017). This study also draws on the ideas from previous modeling works for clouds on brown dwarfs and giant exoplanets, which proposed that radiative cloud feedbacks could drive observed oscillations in these objects’ brightness temperatures (Tan & Showman 2019, 2021a,b).

In the Methods section, we outline the simple model used to demonstrate the magma temperature-cloud feedback and our approach to constraining model parameters using observational data. The Results section describes the self-sustained oscillations of the cloudiness and the surface temperature of the planet, which manifest as variations in the exoplanet’s brightness temperature, as well as how these oscillations change under different conditions. In

Discussions and Conclusion, we assess the potential impact of factors not included in this simple model, identify potential observational discriminants of the proposed mechanism, and suggest directions for future research.

2. METHODS

2.1. Model formulation

We develop a simple box model for the magma temperature-cloud feedback, as shown in Figure 1. Under clear-sky conditions, the stellar radiation flux received by a zero-albedo surface in the substellar region, $S_0 = 3.4 \times 10^6 \text{ W m}^{-2}$, could sustain a magma ocean. We characterize the mean surface temperature of the substellar magma ocean with T_{surf} . Above the magma ocean, the atmosphere consists of non-condensable gases, such as CO_2 , CO , or N_2 . The magma ocean supplies vapor (e.g., SiO) derived from silicates, which can be transported to higher altitudes by substellar convection, where it subsequently condenses to form silicate clouds. The rate of vapor supply increases with T_{surf} . We focus on the surface temperature of the substellar region, rather than the mean surface temperature of the dayside, when formulating the cloud production rate below. We do so as the hottest substellar region is likely the primary source of cloud-forming vapor, given the strong temperature dependence of saturated vapor pressure.

For simplicity, we define “shortwave” radiation as the radiation from the star and “longwave” radiation as the radiation from the surface and cloud. We assume that the cloud scatters shortwave radiation but does not absorb it. We denote the cloud optical depth in the shortwave as τ_{SW} . For longwave radiation, we assume that the cloud absorbs and emits it but does not scatter it. We denote the cloud optical depth in the longwave as τ_{LW} . Neglecting potential changes in cloud particle size, we assume that τ_{SW} and τ_{LW} are proportional to each other:

$$\tau_{\text{LW}} = \beta \tau_{\text{SW}} \quad (1)$$

where β is a fixed parameter. τ_{SW} attenuates the incoming stellar radiation and cools the surface, while the longwave opacity induces a greenhouse effect that warms the surface and reduces the outgoing thermal radiation. The only exception to this simplification is that when diagnosing the planet’s brightness temperature in the visible band, we assume that cloud attenuates surface-emitted visible light by scattering it but not absorbing it.

We formulate the evolution of shortwave cloud optical depth τ_{SW} by the following arguments. For the source, we assume that the conversion rate from cloud-forming vapor to cloud particles scales with the upward vapor flux across the cloud base. Considering a time delay (or “lag” hereafter) d for vapor to ascend from the surface to the cloud base, the upward vapor flux at the cloud base at time t scales with the near-surface upward vapor flux at $t - d$. This flux can be decomposed into the near-surface number density of vapor molecules and ascending velocity. According to the ideal gas law, the near-surface number density of vapor molecules scales with the T_{surf} -dependent partial pressure of the vapor divided by surface temperature T_{surf} . The ascending velocity of the vapor is assumed to scale with the atmospheric scale height divided by the vertical transport timescale, with the former being proportional to the mean atmospheric temperature \bar{T} , and the latter being the lag d . To summarize, the vapor flux across the cloud base is assumed to scale with

$$\frac{N_{\text{A}} \bar{T} p_{\text{ref}}}{g M_{\text{air}} T_{\text{surf}} d} \exp\left(-\frac{T_{\text{ref}}}{T_{\text{surf}}|_{t-d}}\right). \quad (2)$$

where N_{A} is Avogadro’s number, g the gravitational acceleration, M_{air} the mean molar mass of the background atmosphere, and T_{ref} a reference temperature with a corresponding saturated vapor pressure p_{ref} . We denote the surface temperature at $t - d$ as $T_{\text{surf}}|_{t-d}$. A further simplification is to assume that \bar{T}/T_{surf} is approximately constant, given the large variability in the exponential term.

The exponential term is based on the Clausius-Clapeyron equation for phase transition. We obtain p_{ref} and T_{ref} by fitting $p_{\text{ref}} \exp(T_{\text{ref}}/T_{\text{surf}}|_{t-d})$ to the equilibrium vapor pressure at the magma ocean surface. For this fitting we use pressure values calculated by Kite et al. (2016), which used the MAGMA chemical equilibrium code (Fegley & Cameron 1987; Schaefer & Fegley 2004, 2009). p_{ref} and T_{ref} may vary with vapor and magma ocean composition. In this study, we use the values for SiO vapor above a magma ocean with a bulk silicate Earth composition: $p_{\text{ref}} = 8.1 \times 10^{13} \text{ Pa}$ and $T_{\text{ref}} = 7.1 \times 10^4 \text{ K}$. We choose SiO as it is among the most abundant cloud-forming vapors in the atmosphere above a magma ocean with a bulk silicate Earth composition (Schaefer & Fegley 2009; Kite et al. 2016; Mahapatra et al. 2017). Sensitivity tests show that our results are not qualitatively sensitive to the choice of cloud-forming vapor.

Assuming a fixed fraction of vapor condenses as it ascends across the cloud base, the formation rate of condensates integrated over a cloud column, in units of molecules $\text{m}^{-2} \text{ s}^{-1}$, can be approximated as

$$\frac{k_1 N_{\text{A}} p_{\text{ref}}}{g M_{\text{air}} d} \exp\left(-\frac{T_{\text{ref}}}{T_{\text{surf}}|_{t-d}}\right) \quad (3)$$

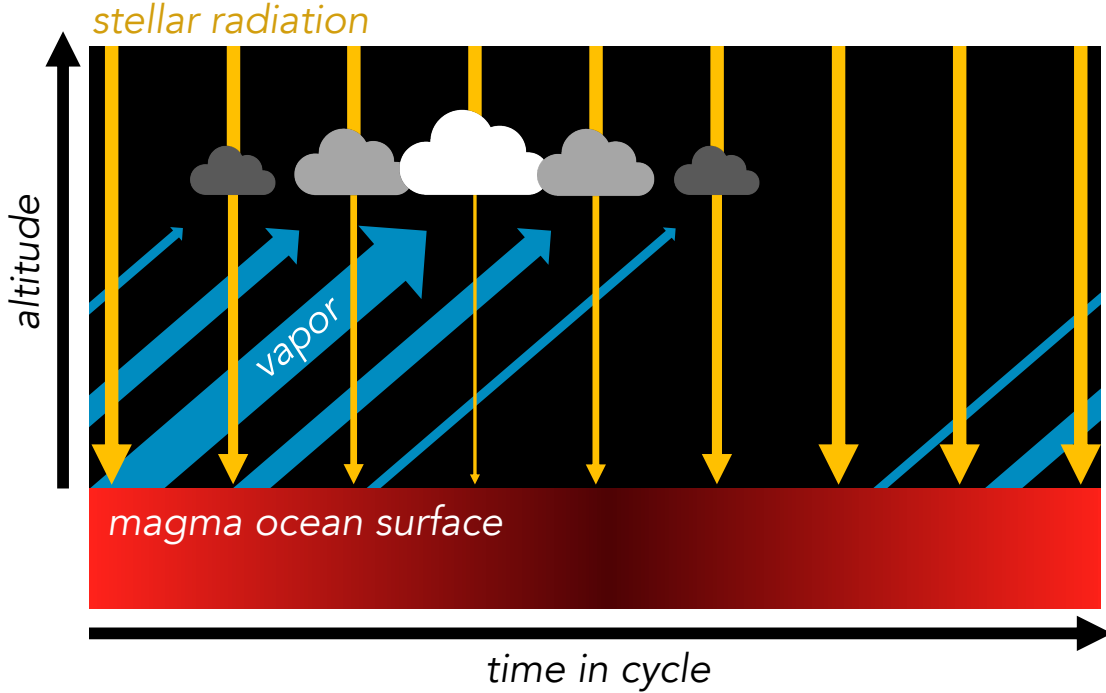


Figure 1. Key elements in the magma temperature-cloud feedback that drives the oscillations in cloudiness and surface temperature. Changes in the color of the magma ocean surface indicate variations in surface temperature (brighter denotes higher temperature). Changes in the brightness of the clouds represent variations in the shortwave opacity of the cloud (brighter denotes higher optical depth). The thicknesses of downward yellow rays indicate shortwave radiation before and after being attenuated by the clouds. The thicknesses of the blue arrows in the upper-right direction indicate ascending vapor fluxes.

where k_1 is a dimensionless scale factor that accounts for uncertainties in this scaling, including those in relative humidity, pressure at the cloud base, rate of mixing during vapor transport, condensation fraction, etc.

To convert the formation rate of condensates into the rate of increase in cloud optical depth, we need to consider the microphysics involved. Assuming the molar mass of the vapor is M_v , we can derive the mass of condensates formed in a cloud column per unit time. With the density of the condensate ρ_c and the mean radius of cloud particles r_c , the mean mass of a spherical cloud particle is approximately $\frac{4}{3}\pi\rho_cr_c^3$, from which we can derive the production rate of cloud particles in a cloud column.

In the shortwave, the extinction cross-section of a single cloud particle is approximately $2\pi r_c^2$ (Pierrehumbert 2010, Chapter 5.4). Therefore, the rate of increase in the extinction coefficient integrated over a cloud column, or the rate of increase in cloud optical depth, is

$$\frac{3k_1 M_v p_{\text{ref}}}{2g M_{\text{air}} \rho_c r_c d} \exp\left(-\frac{T_{\text{ref}}}{T_{\text{surf}}|_{t-d}}\right). \quad (4)$$

We assume the loss term of cloud optical depth scales with cloud optical depth itself, resulting in a “residence time” for cloud particles. We conservatively estimate this residence time assuming cloud loss occurs via particle sedimentation. The residence time is assumed to scale with the atmospheric scale height $R^*T/(M_{\text{air}}g)$ divided by the Stokes falling velocity $2\rho_cr_c^2/(9\eta)$, where η is the dynamic viscosity of the background atmosphere. For simplification, we use a constant characteristic atmospheric temperature T_0 in place of T in the expression for atmospheric scale height. Therefore, the loss rate of cloud optical depth in the shortwave can be expressed as

$$\frac{2k_2 g^2 M_{\text{air}} \rho_c r_c^2}{9R^* T_0 \eta} \tau_{\text{SW}} \quad (5)$$

where k_2 is a dimensionless coefficient accounting for uncertainties in the scaling.

To summarize, the equation that describes the time rate of change of shortwave cloud opacity τ_{SW} is

$$\frac{d\tau_{\text{SW}}}{dt} = \frac{3k_1 M_v p_{\text{ref}}}{2g M_{\text{air}} \rho_c r_c d} \exp\left(-\frac{T_{\text{ref}}}{T_{\text{surf}}|_{t-d}}\right) - \frac{2k_2 g^2 M_{\text{air}} \rho_c r_c^2}{9R^* T_0 \eta} \tau_{\text{SW}}. \quad (6)$$

Thus, the variability in cloudiness is powered by fluctuations in the surface temperature of the substellar magma ocean. Cloud dissipation only responds to cloud formation, relaxing the system towards clear-sky conditions.

To model the evolution of T_{surf} , we consider radiative heating and cooling as well as the effect of latent heat during magma solidification and melting. Given the strong thermal emission at the high temperature, we neglect the effects of sensible heat and latent heat during magma vaporization. In the atmosphere, we only consider the longwave opacity of clouds and neglect the longwave opacity of background gases. Surface radiative heating is from the absorbed stellar shortwave radiation and the downward cloud longwave radiation. With a near-zero surface albedo, as supported by the observed near-zero secondary eclipse depths across visible to near-IR bands, the absorbed shortwave radiation is:

$$\frac{S_0}{1 + \alpha\tau_{\text{SW}}} \quad (7)$$

where $S_0 = 3.4 \times 10^6 \text{ W m}^{-2}$ is the incoming stellar flux at the top of the atmosphere and $1/(1 + \alpha\tau_{\text{SW}})$ accounts for multiple scattering of the cloud. For simplicity, we choose a median value $\alpha = 0.5$. No absorption by cloud is assumed in the shortwave, so the cloud albedo in the shortwave A , which measures the reflected fraction of the total incoming stellar radiation, is

$$A = 1 - \frac{1}{1 + \alpha\tau_{\text{SW}}}. \quad (8)$$

This functional form approximates the derivation of planetary albedo in [Pierrehumbert \(2010\)](#) Chapter 5.6 for conservative scattering and no surface reflection.

We assume that the cloud radiates like a blackbody in the longwave, emitting both upward towards space and downward towards the surface. Given the potential vertical extent of the cloud, we model the cloud's upward emission at a temperature $T_{\text{cloud}\uparrow}$ with emissivity $\varepsilon_{\text{cloud}}$, and its downward emission at a different temperature $T_{\text{cloud}\downarrow}$ with the same emissivity $\varepsilon_{\text{cloud}}$. Modeling the vertical structure of the cloud is beyond the scope of this study, so for simplicity we introduce

$$\Delta T_{\text{cloud}} = T_{\text{cloud}\downarrow} - T_{\text{cloud}\uparrow} \quad (9)$$

as a model parameter to represent the cloud's vertical extent. A larger ΔT_{cloud} corresponds to a larger vertical extent.

Following Beer's law, we represent cloud emissivity as

$$\varepsilon_{\text{cloud}} = 1 - \exp(-\tau_{\text{LW}}) = 1 - \exp(-\beta\tau_{\text{SW}}). \quad (10)$$

Assuming zero surface albedo in the longwave, the downward longwave radiative flux emitted by the cloud and received by the surface is then $\varepsilon_{\text{cloud}}\sigma T_{\text{cloud}\downarrow}^4$, where σ is the Stefan-Boltzmann constant.

The surface cools by emitting longwave radiation as a blackbody at T_{surf} , with an emission flux given by σT_{surf}^4 . We assume that the cloud absorbs a portion of this flux with an absorptivity $\varepsilon_{\text{cloud}}$. Consequently, the energy balance equation for the cloud can be written as:

$$\varepsilon_{\text{cloud}}\sigma T_{\text{surf}}^4 = \varepsilon_{\text{cloud}}\sigma T_{\text{cloud}\uparrow}^4 + \varepsilon_{\text{cloud}}\sigma T_{\text{cloud}\downarrow}^4. \quad (11)$$

This equation indicates that the cloud's emission temperatures, $T_{\text{cloud}\uparrow}$ and $T_{\text{cloud}\downarrow}$, are determined by the variable surface temperature T_{surf} and the static model parameter ΔT_{cloud} .

We assume only a well-mixed surface layer of the magma ocean is thermally influenced by the oscillations. Thus, the evolution of surface temperature is determined by

$$\frac{dT_{\text{surf}}}{dt} = \frac{S_0/(1 + \alpha\tau_{\text{SW}}) + [1 - \exp(-\beta\tau_{\text{SW}})]\sigma T_{\text{cloud}\downarrow}^4 - \sigma T_{\text{surf}}^4}{c_p\rho_m H_{\text{mix}}} \quad (12)$$

where c_p is the specific heat capacity of the magma, ρ_m the magma density, and H_{mix} the thickness of the surface mixed layer. The product $c_p\rho_m H_{\text{mix}}$ is the heat capacity of the surface magma ocean. To account for latent heat release during magma solidification, we do not allow T_{surf} to fall below the solidus temperature $T_{\text{solidus}} = 1400 \text{ K}$ ([Katz et al. 2003](#)) while surface net energy loss occurs. Accordingly, to account for latent heat absorption during magma melting, we hold T_{surf} at T_{solidus} while surface net energy gain occurs until the previously released latent heat is fully absorbed before increasing T_{surf} above T_{solidus} . For the parameters considered here, we find the magma ocean's surface layer never completely solidifies.

Combining Equation (12) with Equation (6), we have formulated a closed set of equations that allows us to predict the behavior of the $T_{\text{surf}}\text{-}\tau_{\text{SW}}$ system. We then nondimensionalize time t against the lag time d , so any potential oscillation period can be expressed as multiples of d . Denoting the dimensionless time as $t' = t/d$, Equations (6) and (12) can then be rewritten as

$$\frac{d\tau_{\text{SW}}}{dt'} = \frac{3k_1 M_v p_{\text{ref}}}{2g M_{\text{air}} \rho_c r_c} \exp\left(-\frac{T_{\text{ref}}}{T_{\text{surf}}|_{t'-1}}\right) - \frac{2k_2 g^2 M_{\text{air}} \rho_c r_c^2 d}{9R^* T_0 \eta} \tau_{\text{SW}} \quad (13)$$

and

$$\frac{dT_{\text{surf}}}{dt'} = \frac{S_0/(1 + \alpha\tau_{\text{SW}}) + [1 - \exp(-\beta\tau_{\text{SW}})] \sigma T_{\text{cloud}\downarrow}^4 - \sigma T_{\text{surf}}^4}{c_p \rho_m H_{\text{mix}}/d}, \quad (14)$$

respectively.

We define three bulk model parameters:

$$\Pi_1 = \frac{3k_1 M_v}{2g M_{\text{air}} \rho_c r_c}, \quad (15)$$

$$\Pi_2 = \frac{2k_2 g^2 M_{\text{air}} \rho_c r_c^2 d}{9R^* T_0 \eta}, \quad (16)$$

and

$$\Pi_3 = \frac{c_p \rho_m H_{\text{mix}}}{d}. \quad (17)$$

Π_1 may be interpreted as a shortwave scatterer (or longwave absorber) productivity, Π_2 as the loss efficiency of shortwave scatterer (or longwave absorber), and Π_3 as a thermal inertia. Equations 13 and 14 can then be rewritten as

$$\frac{d\tau_{\text{SW}}}{dt'} = \Pi_1 p_{\text{ref}} \exp\left(-\frac{T_{\text{ref}}}{T_{\text{surf}}|_{t'-1}}\right) - \Pi_2 \tau_{\text{SW}} \quad (18)$$

and

$$\frac{dT_{\text{surf}}}{dt'} = \frac{S_0/(1 + \alpha\tau_{\text{SW}}) + [1 - \exp(-\beta\tau_{\text{SW}})] \sigma T_{\text{cloud}\downarrow}^4 - \sigma T_{\text{surf}}^4}{\Pi_3}, \quad (19)$$

respectively.

We then analyze the solutions to the equations above (with the additional constraint that T_{surf} cannot fall below T_{solidus}) for various values of the bulk model parameters Π_1 , Π_2 , and Π_3 , as well as β and ΔT_{cloud} . Through numerical simulations, we identify regions in the parameter space where T_{surf} and τ_{SW} exhibit oscillations that can induce the observed variability in secondary eclipse depths. The parameter space is explored within the bounds listed in Table 1. The limits for the bulk parameters Π_1 , Π_2 , and Π_3 are derived from the estimated bounds of individual model parameters (such as ρ_c , r_c , c_p , and H_{mix} , see Appendix). We set the upper bound for ΔT_{cloud} based on the difference between the atmosphere's emission temperature and the stratospheric skin temperature, assuming the former is equal to the highest observed 4.5 μm brightness temperature from Patel et al. (2024). The β parameter is influenced by multiple factors, with cloud particle size likely being the most critical. We explore $10^{-3} < \beta < 1$ to represent varying degrees of cloud longwave emissivity, along with $\beta = 0$, which corresponds to no cloud longwave emissivity. With $\beta = 0$, ΔT_{cloud} has no effect in the model, reducing the five-dimensional parameter space to three-dimensions (spanned solely by Π_1 , Π_2 , and Π_3).

Table 1. Estimated bounds for the model parameters that span the parameter space.

parameter	lower bound	upper bound	unit	note
Π_1	$10^{-3.20}$	$10^{2.41}$	Pa^{-1}	
Π_2	$10^{-7.34}$	$10^{3.71}$	dimensionless	
Π_3	$10^{0.439}$	$10^{6.26}$	$\text{kg s}^{-3} \text{K}^{-1}$	
ΔT_{cloud}	0	350	K	
β	10^{-3}	1	dimensionless	$\beta = 0$ is also explored.

2.2. Numerical method to solve the equations

We solve Equations (18) and (19) for T_{surf} and τ_{SW} with a stiffly-accurate fourth-order explicit singly diagonal implicit Runge-Kutta (ESDIRK) method (Kennedy & Carpenter 2003) using the Julia differential equation solving ecosystem DifferentialEquations.jl (Rackauckas & Nie 2017; Widmann & Rackauckas 2022). Between $t' = 0$ and $t' = 1$, we fix $T_{\text{surf}}|_{(t'-1)}$ at the initial temperature value but let τ_{SW} and T_{surf} vary according to the two equations.

We find that for the parameter space of Table 1, all solutions reach a steady state at the fixed point $(T_{\text{surf}}^*, \tau_{\text{SW}}^*)$, which depends on the model parameters, or oscillate on a stable limit cycle on the phase diagram (see an example in Figure 2). For a given parameter set, we solve for the fixed point $(T_{\text{surf}}^*, \tau_{\text{SW}}^*)$ numerically by setting the left-hand sides of Equations (18) and (19) equal to zero. When the solution leads to a limit cycle, this fixed point is unstable with the limit cycle encircling it.

During integration, we check if a solution is in steady state, in a limit cycle, or neither, by considering integration steps within the previous 100 units of the nondimensionalized time t' , which is longer than any limit cycle periods we detect. If the maximum and minimum surface temperatures within this duration are equal to T_{surf}^* within ± 1 K, we consider the solution in steady state. If not, we search for all times T_{surf} crosses T_{surf}^* . From these T_{surf}^* crossings, we calculate periods of oscillations about T_{surf}^* . We consider the solution to be in a limit cycle if these periods do not significantly vary, or specifically, if the standard deviation of all periods calculated over the previous 100 units of t' is less than 1% of the mean period. In all other scenarios, we consider the solution to still be evolving.

2.3. Brightness temperature calculation and model-observation comparisons

We investigate what portion of the plausible parameter space of Table 1 can lead to limit-cycle oscillations that are consistent with the observed variability in the $4.5 \mu\text{m}$ brightness temperature (Demory et al. 2016a; Tamburo et al. 2018; Patel et al. 2024). To efficiently sample this five-dimensional parameter space, we use Latin hypercube sampling (McKay et al. 2000) of $\log \Pi_1$, $\log \Pi_2$, $\log \Pi_3$, ΔT_{cloud} , and $\log \beta$ within the bounds presented in Table 1. Latin hypercube sampling divides each parameter range into equally spaced bins, randomly samples one point from each bin, and then randomly combines samples of different parameters to generate parameter sets. For each parameter set, we solve the equations for T_{surf} and τ_{SW} until their solution reaches a final state, either a steady state or a limit cycle.

At $4.5 \mu\text{m}$ (in the longwave), reflection by cloud is negligible, so we calculate the brightness temperature for the substellar region $T_{\text{b},4.5}$ following the equation below:

$$B(T_{\text{b},4.5}, \lambda = 4.5 \mu\text{m}) = B(T_{\text{surf}}, \lambda = 4.5 \mu\text{m}) \exp(-\tau_{\text{LW}}) + B(T_{\text{cloud}\uparrow}, \lambda = 4.5 \mu\text{m}) [1 - \exp(-\tau_{\text{LW}})] \quad (20)$$

where $B(T, \lambda)$ is the Planck function for a blackbody with temperature T at wavelength λ .

We apply Equation (20) to final-state time series of T_{surf} , τ_{LW} , and $T_{\text{cloud}\uparrow}$, and calculate the lowest and the highest $T_{\text{b},4.5}$ for each parameter combination. We then assess if a parameter combination can produce a solution consistent with observations by comparing the modeled highest and lowest $T_{\text{b},4.5}$ with the observed values (Demory et al. 2016a; Tamburo et al. 2018; Patel et al. 2024). Considering the reported uncertainties in the observed brightness temperatures, we classify the parameter space into 1σ , 2σ , and 3σ tiers, corresponding to agreement with both the deepest and shallowest secondary eclipse depth observations within one, two, and three times the measurement errors, respectively. The highest disk-mean brightness temperature of the dayside at $4.5 \mu\text{m}$ is no lower than 2448 K, 2080 K, and 1712 K within one, two, and three times the measurement errors, respectively, as reported by the fifth data point in Table 4 of Demory et al. (2016a). These lower bounds on the highest disk-mean brightness temperature of the dayside can also serve as lower bounds for the highest brightness temperature of the substellar region, as the latter is probably higher. The lowest disk-mean brightness temperature of the dayside at $4.5 \mu\text{m}$ is no higher than 1040 K, 1207 K, and 1374 K within one, two, and three times the measurement errors, respectively, as indicated by the first data point in Table 1 of Patel et al. (2024). However, these upper bounds can not be directly applied to the probably higher lowest brightness temperature of the substellar region. The maximum difference between the substellar brightness temperature and the disk-mean brightness temperature of the dayside might occur on a 1:1 tidally locked planet without an atmosphere to redistribute heat. On such a planet, assuming a fully absorbing Lambertian surface, the substellar surface temperature is $\sim 10\%$ higher than the disk-mean surface temperature of the dayside. Using this as a reference, we adjust the upper bounds on the lowest brightness temperature of the substellar region by a factor of 1.1, resulting in values of 1144 K, 1328 K, and 1511 K for 1σ , 2σ , and 3σ observational consistency, respectively.

Due to the challenge of distinguishing between the contributions of reflected starlight and the planet's thermal emission in the observed brightness temperature in the visible and near-IR bands, we do not assess the consistency

of model outputs with observations based on the brightness temperatures in these bands (Meier Valdés et al. 2022; Demory et al. 2023; Patel et al. 2024). However, we compute the modeled brightness temperature in the visible band to illustrate that it can oscillate out of phase with the modeled brightness temperature in the mid-IR (e.g., at 4.5 μm wavelength). The brightness temperature at 0.5 μm , $T_{\text{b},0.5}$, is calculated using the following equation:

$$B(T_{\text{b},0.5}, \lambda = 0.5 \mu\text{m}) = A \times B(T_{\text{star}}, \lambda = 0.5 \mu\text{m}) \times \frac{R_{\text{star}}^2}{a^2} + (1 - A) \times B(T_{\text{surf}}, \lambda = 0.5 \mu\text{m}) \quad (21)$$

where $T_{\text{star}} = 5172$ K is the effective temperature of the host star (Bourrier et al. 2018b), $R_{\text{star}} = 6.56 \times 10^8$ m is the radius of the host star (von Braun et al. 2011), $a = 2.33 \times 10^9$ m is the semi-major axis of the planet’s orbit (Dawson & Fabrycky 2010), and A is the shortwave albedo in Equation (8). The first term represents the reflected starlight, while the second term accounts for thermal emission from the planetary surface that penetrates through the cloud. At visible wavelengths, clouds attenuate surface-emitted radiation by scattering it, which is why the cloud’s shortwave albedo is included here.

3. RESULTS

3.1. Oscillations in brightness temperature and their underlying mechanisms

Limit-cycle oscillations in surface temperature (T_{surf}) and shortwave cloud optical depth (τ_{SW}) occur within certain regions of the parameter space defined in Table 1. Figure 2 illustrates an example. In the phase diagram for T_{surf} and τ_{SW} (Fig. 2A), the limit cycle is represented by a closed loop. If the system’s state starts inside the loop, it spirals outward until it converges on the loop; if it starts outside, it spirals inward to the loop. A state initiated exactly on the loop remains there indefinitely. These behaviors demonstrate that the closed loop is a stable limit cycle and that the system’s oscillations on this loop are an intrinsic characteristic of its dynamics. Inside the loop, there is a fixed point. The system’s state remains unchanged if initiated at this point, but any deviation from the fixed point will automatically amplify, driving the system towards the limit cycle. This indicates that the fixed point is unstable. Given external perturbations in the real world, this instability suggests that no steady state can exist in these regions of the parameter space.

As shown in Fig. 2, a typical limit cycle can be divided into four stages:

Stage 1: The system is nearly cloud-free, with the surface receiving unattenuated stellar radiation. The surface stays at its highest temperature to balance the heating from stellar radiation with cooling through thermal emission. This hot-surface, cloud-free state typically lasts for a duration between d and $2d$, appearing as a point in Fig. 2A and nearly horizontal lines in Figs. 2C and 2D. During this stage, the evaporation of silicates, which supplies cloud-forming vapor, is strong, but the vapor has not yet reached the colder, cloud-forming regions due to lagged atmospheric transport.

Stage 2: This stage begins when the vapor reaches the cold regions where the vapor condenses, ultimately leading to an increase of cloudiness over the substellar region. This stage corresponds to the sudden rise in cloud optical depth in Figs. 2A and 2D. The increased cloud albedo reflects a significant portion of stellar radiation, reducing the energy absorbed by the surface and cooling the surface.

Stage 3: The cloud optical depth remains at its maximum (Figs. 2A and 2D), minimizing the amount of stellar radiation reaching the surface. As a result, surface cooling persists. Following the Clausius-Clapeyron relationship, the decrease in surface temperature lowers the saturated vapor pressure, significantly reducing vapor supply from evaporation. However, the cloud does not immediately respond due to the time lag in vapor transport from the substellar magma ocean surface to the cloud formation zone. This stage typically lasts longer than d .

Stage 4: The surface cooling effect eventually reaches the cloud-forming regions, causing a rapid decline in cloud formation. As clouds fade out by particle sedimentation, the atmosphere returns to a clear-sky condition. With the clouds dissipating, more stellar radiation reaches the surface, which warms. This stage ends when the clouds have almost disappeared and the surface temperature has risen sufficiently to balance incoming shortwave radiation through thermal emission under clear skies, marking the start of the next cycle.

With the assumed linear relationship between longwave and shortwave cloud optical depths in Equation 1, the longwave cloud optical depth also increases during Stage 2 (Fig. 2D), enhancing the greenhouse effect that warms the surface. However, this warming effect is transient. As the surface cools, thermal emission from the surface, which provides the energy sustaining the cloud’s temperature, also declines. Consequently, the cloud cools with the cooling surface (Fig. 2C), reducing surface warming by cloud longwave radiation. In most cases, surface heating by cloud

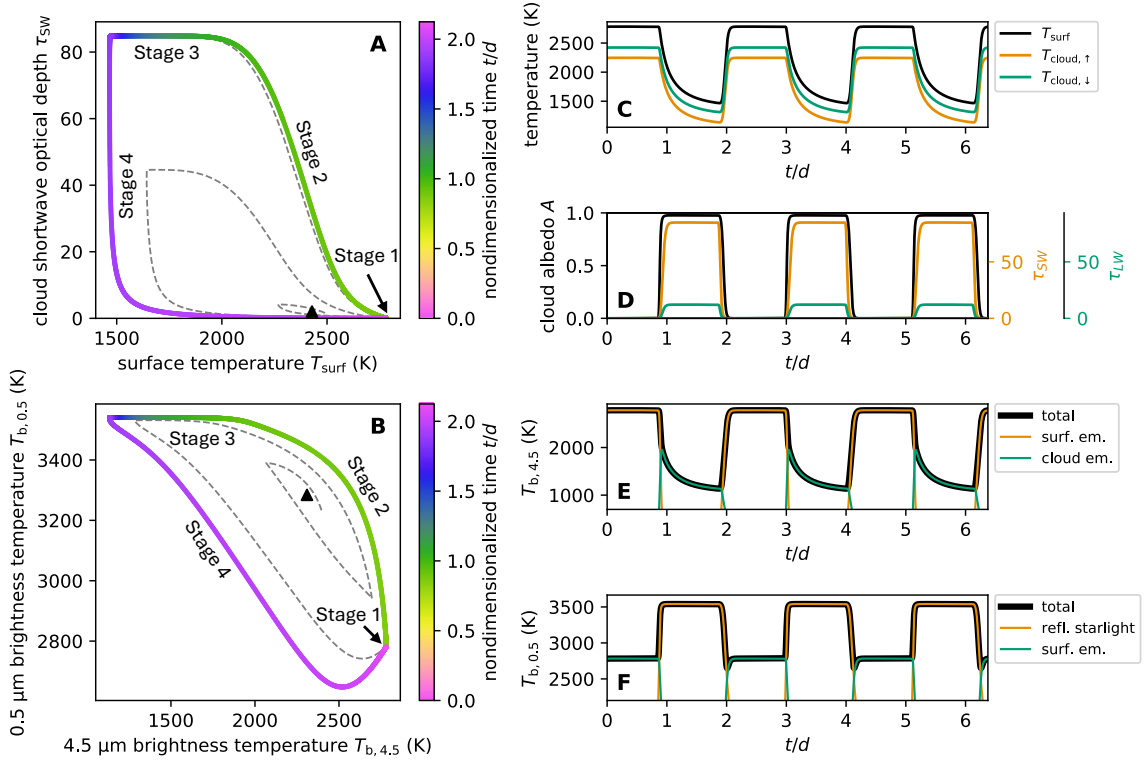


Figure 2. An example of simulated limit-cycle oscillations in surface temperature (T_{surf}) and shortwave cloud optical depth (τ_{SW}) in the substellar region, which manifest as oscillations in substellar brightness temperature at $4.5 \mu\text{m}$ in the mid-IR band ($T_{b,4.5}$) and at $0.5 \mu\text{m}$ in the visible band ($T_{b,0.5}$). **(A)** Phase diagram of T_{surf} and τ_{SW} , where the trajectory of the system’s state vector (dashed curve) converges towards a closed loop (colored curve) while spiraling counter-clockwise, indicating a stable limit cycle. Colors represent nondimensionalized time over the course of one cycle period. The black triangle marks the unstable fixed point. **(B)** Similar to **(A)**, but for the $4.5 \mu\text{m}$ brightness temperature $T_{b,4.5}$ and the $0.5 \mu\text{m}$ brightness temperature $T_{b,0.5}$. **(C)** Time series of surface temperature T_{surf} (black), cloud upward emission temperature $T_{\text{cloud}, \uparrow}$ (orange), and cloud downward emission temperature $T_{\text{cloud}, \downarrow}$ (green) over three cycles. **(D)** Similar to **(C)**, but showing shortwave cloud albedo A (left y-axis, black), shortwave cloud optical depth τ_{SW} (right y-axis, orange), and longwave cloud optical depth τ_{LW} (right y-axis, green). **(E)** Time series of brightness temperature at $4.5 \mu\text{m}$. The black curve represents the brightness temperature resulting from the combined thermal emission from the surface and the cloud. The orange curve shows only surface emission penetrating the cloud, and the green curve shows only cloud emission. **(F)** Similar to **(E)**, but for the brightness temperature at $0.5 \mu\text{m}$. The black curve represents the brightness temperature resulting from the combined reflected starlight and surface thermal emission, while the orange and green curves represent reflected starlight and surface thermal emission, respectively. Model parameters: $\Pi_1 = 9.47 \text{ Pa}^{-1}$, $\Pi_2 = 74.2$, $\Pi_3 = 115 \text{ kg s}^{-3} \text{ K}^{-1}$, $\Delta T_{\text{cloud}} = 177 \text{ K}$, and $\beta = 0.143$.

thermal emission is relatively minor compared to the heating from absorbed stellar radiation and the cooling from surface thermal radiation throughout the cycle.

The oscillations in surface temperature and cloud optical depth drive corresponding fluctuations in brightness temperature in both mid-IR and visible bands (Figs. 2B, 2E, and 2F). We focus on $4.5 \mu\text{m}$ for the mid-IR ($T_{b,4.5}$) and $0.5 \mu\text{m}$ for the visible band ($T_{b,0.5}$) to illustrate these processes.

Stage 1: During this stage, the surface is at its hottest state, and the atmosphere is nearly cloud-free. Almost all of the strong thermal emission from the surface escapes directly to space, resulting in $T_{b,4.5}$ being at its peak, closely matching the surface temperature (about 2780 K, Figs. 2B and 2E). In contrast, $T_{b,0.5}$ is near its minimum (about 2780 K) because, without reflective clouds, no starlight is reflected, so $T_{b,0.5}$ also aligns with the surface temperature (Figs. 2B and 2F).

Stage 2: As cloud optical depth increases rapidly, the surface temperature plummets. This leads to a quick decline in $T_{b,4.5}$ as the mid-IR emission level rises from the surface to the cloud-top (Fig. 2E). Simultaneously, $T_{b,0.5}$ rises due to increased cloud albedo reflecting more starlight (Fig. 2F).

Stage 3: The cloud optical depth remains high while surface and cloud temperatures continue to fall. This causes a continued decline in $T_{b,4.5}$, as it is now dominated by thermal emission from the cloud (Fig. 2E). In contrast, $T_{b,0.5}$ stays at its peak due to the constant stellar radiation and stable cloud albedo (Fig. 2F).

Stage 4: Cloud optical depth decreases rapidly, exposing the surface, and surface temperature begins to rise again, dominating $T_{b,4.5}$. As the surface re-heats from stellar radiation, $T_{b,4.5}$ increases quickly (Fig. 2E). Meanwhile, $T_{b,0.5}$ drops rapidly as the reflective cloud disperses, reducing the contribution from reflected starlight (Fig. 2F). Towards the end of Stage 4, some parameter combinations produce cycles with a brief dip in $T_{b,0.5}$ because the surface temperature does not rise fast enough to compensate for the reduced reflected starlight.

In many cases, $T_{b,4.5}$ and $T_{b,0.5}$ oscillate out of phase (Fig. 2B). Typically, the highest $T_{b,4.5}$ occurs when $T_{b,0.5}$ is near its lowest value, both corresponding to cloud-free conditions. As cloud cover increases, $T_{b,0.5}$ reaches its peak due to maximum cloud albedo, while $T_{b,4.5}$ continues to fall as the cloud and surface cool. This out-of-phase behavior is found across a broad parameter space where oscillations occur, though the exact phase difference between $T_{b,4.5}$ and $T_{b,0.5}$ oscillations depends on specific model parameters. The near-IR brightness temperature, observed at 2.1 μm by JWST (Patel et al. 2024), lies between the mid-IR and visible bands and is also expected to oscillate out of phase with visible and mid-IR brightness temperatures. However, detailed modeling based on wavelength-dependent optical properties of silicate clouds is out of the scope of this study.

3.2. Impact of model parameters on model-observation consistency

Figure 3 illustrates regions of the parameter space (Table 1) where limit-cycle oscillations can reproduce the observed highest and lowest 4.5 μm brightness temperatures (Demory et al. 2016a; Patel et al. 2024). A substantial range of model parameters is capable of reproducing the observed magnitude of the 4.5 μm brightness temperature variability. Favorable conditions for reproducing the observed oscillations include a large Π_1 , an intermediate Π_2 , a small Π_3 , and a large ΔT_{cloud} in the presence of longwave cloud effects ($\beta > 0$).

Model-observation consistency requires that Π_1 , which governs vapor supply and cloud formation, is not too small, because insufficient cloud formation fails to reduce surface heating by stellar radiation in Stage 2. An intermediate Π_2 , which corresponds to an intermediate cloud removal rate, is also required. If Π_2 is too small, clouds persist too long, damping oscillations in cloud optical depth and reducing their amplitude. Conversely, if Π_2 is too large, limited cloudiness resulting from rapid cloud removal prevents sufficient surface cooling, making it hard to match the observed lowest 4.5 μm brightness temperature. A small Π_3 helps sustain large-amplitude oscillations by allowing fast surface temperature response to imbalances in the surface energy budget. If Π_3 is too large, surface temperature oscillations are dampened, resulting in small oscillation amplitude.

The model parameter β , which represents the ratio of longwave to shortwave cloud optical depth, affects the strength of the cloud greenhouse effect. β generally has a small impact as long as $\beta > 10^{-3}$, except when Π_1 is small or Π_2 is large. In such cases, limited cloud formation or rapid cloud removal leads to limited cloudiness, so a larger β —indicating a higher capability of a single cloud particle to absorb longwave radiation—allows stronger absorption of surface radiation by cloud, thereby enhancing the greenhouse effect and helping to reduce $T_{b,4.5}$ to the observed values (Patel et al. 2024). Notably, in the absence of longwave cloud absorptivity and emissivity ($\beta = 0$), surface thermal emission alone can reproduce the observations within 3σ in some regions of the parameter space. However, the solidus temperature of the magma imposes a lower limit on the surface temperature, preventing 2σ consistency with the lowest observed $T_{b,4.5}$ from Patel et al. (2024). Achieving 2σ and 1σ model-observation consistency requires the cloud to absorb thermal radiation from the surface and re-emit it at a lower temperature.

With longwave cloud absorptivity and emissivity ($\beta > 0$), the parameter ΔT_{cloud} , which represents the difference between the cloud’s downward and upward emission temperatures (largely influenced by cloud layer thickness), also impacts the mid-IR brightness. If ΔT_{cloud} is too small, the cloud-top temperature remains too high, meaning that even if all surface radiation is absorbed by the cloud, the cloud’s own thermal emission could result in $T_{b,4.5}$ significantly higher than the observed minimum.

Figure 3 also shows that a smaller Π_2 can offset the effects of a smaller Π_1 . When vapor supply and cloud formation are inefficient (small Π_1), a slower cloud particle sedimentation rate or longer cloud residence time (small Π_2) can sustain higher cloudiness, which helps sufficiently cool the surface. However, as previously noted, Π_2 cannot be too small, as long-lived clouds would dampen the oscillations.

The lag, d , in the response of cloudiness to surface temperature also affects the model’s oscillations by influencing Π_2 and Π_3 . A larger d results in a larger Π_2 and a smaller Π_3 . The former can improve model-observation consistency

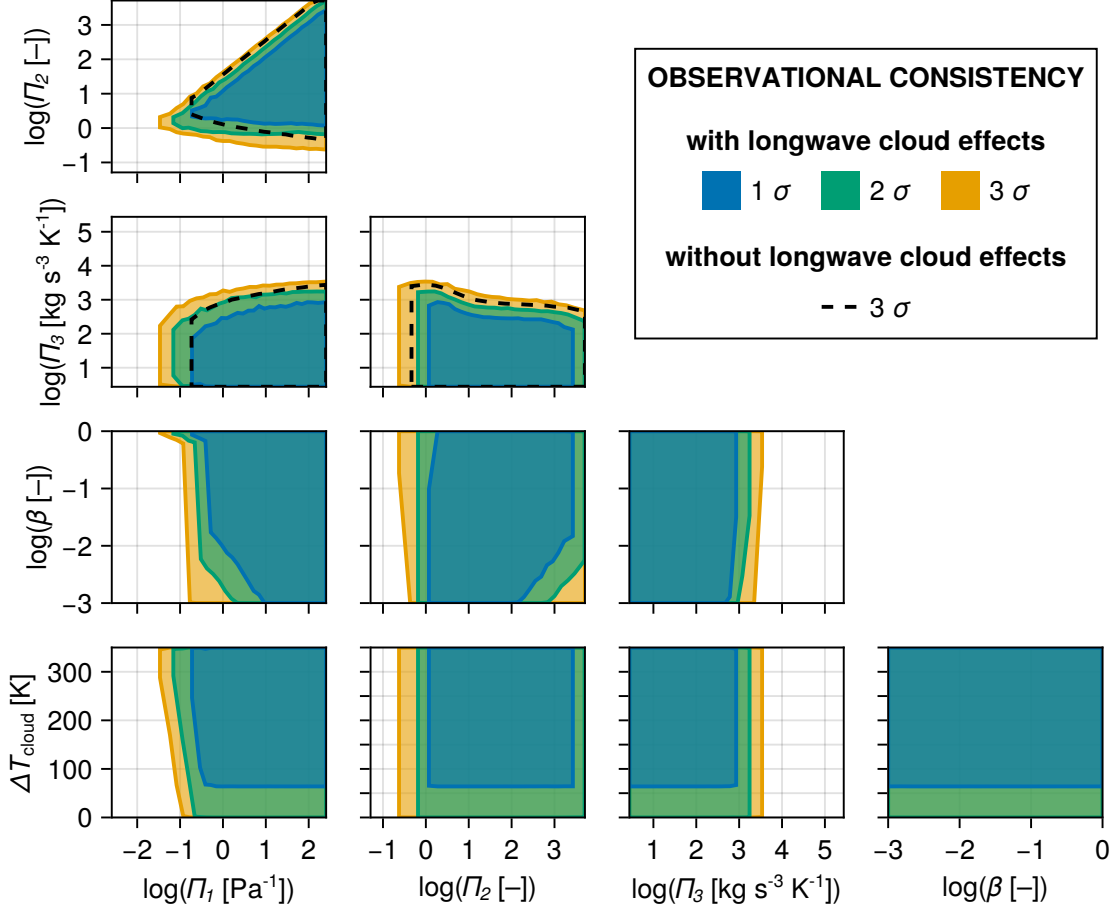


Figure 3. Parameter ranges capable of simultaneously reproducing the upper and lower bounds of Spitzer and JWST $4.5 \mu\text{m}$ brightness temperature observations within one, two, and three times the measurement uncertainty (σ). The shading and solid contours show the model with longwave cloud effects ($10^{-3} < \beta < 1$). Different colors indicate different levels of consistency. The dashed contours in the first two rows show the model without longwave cloud effects ($\beta = 0$) at 3σ model-observation consistency. No 2σ consistency can be achieved without longwave cloud effects. Each panel shows a two-dimensional (2D) projection of the 5D (for $10^{-3} < \beta < 1$) or 3D (for $\beta = 0$) parameter space defined in Table 1. A location in each 2D projection is classified into a given consistency tier if, for the two parameters plotted, there exist values of the other parameters (within their respective bounds) that can produce oscillations consistent with observations at that consistency tier. Consistency between the model and observations is achieved across a substantial subset of the parameter space.

at small Π_2 , but reduce consistency at large Π_2 . A smaller Π_3 can enhance consistency because a longer lag allows the surface more time to heat before the cloud optical depth increases and more time to cool before the cloud optical depth decreases, leading to higher-amplitude oscillations. In order for the oscillations to occur, d must not be too small, as a small d can result in a Π_2 that is too small and a Π_3 that is too large, with the former leading to cloudiness that changes too slowly and the latter causing surface temperatures to vary only slightly before the response in cloudiness, both of which dampen the oscillation amplitude.

The oscillation period ranges from $2d$ to $10d$ for oscillations consistent with observations within 3σ and 2σ , and from $2d$ to $8d$ for those within 1σ . Among the model parameters, Π_2 has the strongest effect on the oscillation period, with smaller values of Π_2 resulting in longer periods. This is because a smaller Π_2 increases the cloud residence time, extending the duration of Stage 4 (during which cloud particle sedimentation occurs). Similarly, Π_3 also affects the oscillation period, with larger Π_3 leading to longer periods. A larger Π_3 slows the rate of surface temperature change, lengthening Stages 2, 3, and 4.

4. DISCUSSION

4.1. *Model limitations*

We presented a simple model of a magma temperature-cloud feedback that can explain the observed brightness temperature oscillations on 55 Cancri e. Many complex processes, (e.g., atmospheric dynamics, magma ocean dynamics, cloud microphysics) which can be represented in more sophisticated, higher-dimensional models, have been omitted or simplified.

The model simplifies the vapor transport from the substellar magma ocean surface, where silicate-derived vapor is supplied to the atmosphere through partial vaporization of magma, to the cloud-forming region. This process is treated as vertical transport. In reality, however, strong horizontal winds may play a significant role in the vapor transport. Earlier works predict wind speeds ranging from 0.2 km s^{-1} to 2 km s^{-1} (Hammond & Pierrehumbert 2017; Nguyen et al. 2020; Fan et al. 2022). According to general circulation models (GCMs), these strong winds likely shear the ascending motion above the substellar region eastward, causing clouds to form primarily near the eastern terminator of the dayside, where temperature is significantly lower than the substellar region. In this scenario, clouds would no longer immediately affect the stellar radiation reaching the surface after their formation. Instead, they may be transported to the nightside by westerlies and then return to the dayside across the western terminator, after which they could eventually reach the substellar region and attenuate incoming stellar radiation.

Even within the simplified vertical transport framework, additional assumptions are made. The model characterizes the ascent of vapor from the magma ocean surface to the cloud base using an ascending velocity that is proportional to the atmospheric scale height and inversely proportional to a constant vertical transport timescale. In reality, convective updrafts are influenced by other factors such as surface heating, atmospheric stability, large-scale forcings, and turbulent mixing—processes that can only be treated in high-resolution higher-dimensional models. For example, the transport timescale d is not constant; during surface cooling, increased atmospheric stability can inhibit convective vapor transport. Conversely, during surface heating, the transport timescale may rapidly shorten as convection resumes (e.g., Colby 1984). Thus, the assumption of a constant transport timescale likely produces oscillations that are smoother than those expected in reality.

The heat capacity of the mixed layer of the surface magma ocean is poorly constrained. Moreover, it may significantly vary as surface heating and cooling change mixed layer thickness over an oscillation period. At high surface temperatures, the thin mixed layer and the resulting small heat capacity of the surface magma ocean could allow a rapid increase in surface temperature and thus a surge in the supply of silicate vapor. Therefore, the assumption of a constant mixed layer depth also likely results in smoother oscillations than in reality. Moreover, Kite et al. (2016) show that under some circumstances, the magma pool surface can be both time-variable and compositionally variegated (patchy). A dynamical magma ocean model coupled to surface forcings (Lai et al. 2024b) will be needed to simulate the ocean mixed layer with better accuracy.

Additionally, our model neglects the longwave opacity of background gases in the atmosphere, despite recent evidence of its presence from absorption features in the $4.5 \text{ }\mu\text{m}$ band (Hu et al. 2024, also see Patel et al. 2024 for a different opinion). This longwave opacity could potentially warm the magma. Atmospheric opacity at $4.5 \text{ }\mu\text{m}$ can also influence the $4.5 \text{ }\mu\text{m}$ brightness temperature. Whether this opacity increases or decreases the observed brightness temperature may depend on the vertical temperature gradient at the $4.5 \text{ }\mu\text{m}$ emission level.

Our model omits horizontal variations in surface temperature and cloud distribution. If different regions on the dayside undergo unsynchronized limit cycles, the overall observable effect could be diminished. However, we consider such asynchrony unlikely, as the $0.2\text{--}2 \text{ km s}^{-1}$ winds (Hammond & Pierrehumbert 2017; Nguyen et al. 2020)—would likely distribute clouds and their cooling effects efficiently, thereby synchronizing the limit cycles across different regions.

4.2. *Tests*

We have shown that the magma temperature-cloud feedback can induce oscillations in the brightness temperature of 55 Cancri e (Figs. 2B, 2E, and 2F), potentially explaining observational data. In the mid-IR (e.g., $4.5 \text{ }\mu\text{m}$), the highest brightness temperature in the substellar region can reach $\sim 2780 \text{ K}$, corresponding to the maximum surface temperature after an extended period of clear-sky conditions. The lowest brightness temperature of the substellar region can be as low as $\sim 960 \text{ K}$, which corresponds to the lowest cloud top emission temperature resulting from the lowest surface temperature (set by T_{solidus} here) after an extended cooling period with maximum cloudiness. Since

the substellar region is likely the hottest area on the dayside, the disk-averaged dayside brightness temperature, which manifests as secondary eclipse depths, is expected to be lower than these values.

At 0.5 μm in the visible band, the highest brightness temperature in the substellar region can reach ~ 3500 K, corresponding to nearly full reflection of starlight at maximum cloud reflectivity. The lowest brightness temperature in the substellar region corresponds to the lowest surface temperature immediately after cloud dispersion which exposes the surface, which we find to be higher than ~ 1400 K for models that align with the mid-IR observations. As reflected starlight could make a significant contribution to the planet’s brightness in the shortwave and the associated secondary eclipse depth, estimating the oscillation amplitudes of these two quantities requires knowledge about the horizontal distribution of reflective cloud over the dayside and wavelength-dependent cloud particle optical properties, including the intensity of backscattering. As our simple model does not predict these effects, it is challenging to make predictions for the planet’s shortwave brightness temperature and secondary eclipse depths. Higher-dimensional simulations that couple silicate cloud evolution with a surface magma ocean are needed to better constrain cloud spatial and temperature distributions as well as cloud particle composition and shape. Because small changes in composition can lead to large changes particle optical properties (Zeidler et al. 2011), laboratory experiments that measure composition and optical properties of particles formed from vaporized magma are highly desirable (e.g., He et al. 2024). Such future modeling and experimental efforts will enable more detailed predictions of the magma temperature-cloud feedback’s implications for shortwave brightness temperature and secondary eclipse depth.

Still, within the framework of our proposed mechanism, we can estimate an upper bound for the secondary eclipse depth in the shortwave where reflected starlight dominantly contributes. If cloud scatters starlight like a Lambertian surface, the geometric albedo due to cloud reflectivity cannot exceed 1, corresponding to a secondary eclipse depth less than ~ 30 ppm at all wavelengths in the shortwave. Our model predicts a negligible contribution from the planet’s thermal emission to the visible-band brightness during time periods with maximum cloudiness. Therefore, our proposed mechanism cannot produce broad-band shortwave secondary eclipse depths higher than ~ 30 ppm, unless silicate clouds backscatter more strongly than a Lambertian surface. The majority of the observed secondary eclipse depths in Meier Valdés et al. (2022) and Demory et al. (2023) are compatible with this upper bound within twice observational uncertainty, but the high outlier (> 50 ppm) eclipse depths reported in Demory et al. (2023), if confirmed, could pose a challenge to cloud and surface temperature variability as the sole explanation for the observed secondary eclipse depth variability. However, we note that our radiation-dominant cloud temperature model might have neglected important heat sources, such as latent heat release during condensation, so the cloud top temperature is likely higher than predicted by our model. The resulting stronger thermal emission from the cloud could enhance the planet’s brightness in CHEOPS’s band pass (400 nm–1 μm), especially in the near-IR, if cloud emissivity dominates over reflectivity there.

Our model predicts out-of-phase oscillations in brightness temperature across different spectral bands. The lowest brightness temperature in the visible band typically occurs around the same time as the peak brightness temperature in the mid-IR band, while the highest visible brightness temperature tends to occur during the decreasing phase of the mid-IR brightness temperature. We also expect the brightness temperature in the near-IR band to oscillate out of phase with visible-band and mid-IR brightness temperature, as observed by Patel et al. (2024), but detailed modeling requires knowledge about wavelength-dependent emissivity and reflectivity of cloud.

The oscillation period predicted by our model is typically several times longer than the lag between the surface temperature maximum and the subsequent increase in cloudiness. This lag could be as short as the vertical transport timescale from the magma ocean surface to the cloud condensation level, likely on an hourly timescale. In such a case, the model’s oscillation period would be short, and brightness temperature variations could be partially smoothed out during the 1.6-hour secondary eclipse. However, in a scenario where ascending vapor is sheared eastward by strong westerly winds, delaying cloud formation over the substellar region, the lag could extend to about ten days. This estimate comes from dividing the planet’s size by the slowest wind speeds (Hammond & Pierrehumbert 2017), as clouds forming on the eastern dayside would need to travel to the nightside and return to the dayside before covering the substellar region. Such a scenario would require an extended cloud residence time compared to the lag, which corresponds to a relatively small Π_2 . Abundant background atmospheric gases such as N_2 , CO , and CO_2 are likely necessary. The observed sub-weekly-timescale brightness temperature variability (Patel et al. 2024) suggests a timescale that lies between the oscillation periods derived from these bounds on the lag. Other processes, such as the breaking of a near-surface convective inhibition layer at the onset of surface warming (Colby 1984) or the nucleation of cloud particles (Lee et al. 2018; Helling 2019), are also expected to influence the lag and hence the oscillation period.

If clouds have a sufficiently long residence time, they could be transported to the nightside, allowing the oscillating cloudiness over the substellar region from our model to manifest as oscillating cloud coverage on the nightside as well. If these clouds have infrared opacity, the oscillating cloudiness on the nightside could lead to fluctuations in the nightside brightness temperature, if nightside cloud temperature differs from nightside surface temperature. Such variations could potentially be detected by future JWST observations of the planet’s phase curve.

Additionally, clouds transported from the nightside to the dayside by westerlies could lead to increased cloud coverage and optical depth over the western dayside, due to cloud sedimentation and re-evaporation during further eastward transport over the dayside, or simply due to the transport timescale across the dayside. This increased cloud coverage on the western dayside would result in higher brightness temperatures in the visible band due to enhanced reflection of starlight, as detected in [Morris et al. \(2021\)](#). If the clouds have infrared opacity, they would absorb surface thermal radiation in the mid-IR band, leading to lower brightness temperatures on the western dayside and creating an apparent eastward “hot spot shift,” as observed by [Demory et al. \(2016b\)](#). These effects could cause asymmetry in the planet’s phase curve. If such asymmetry exists, it is likely to be observable only during phases of the oscillation cycle with high cloudiness.

In summary, our model predicts phase curve asymmetry of varying intensity in both the visible and mid-IR bands: the highest brightness temperature in the visible band would predominantly shift westward, while in the mid-IR band, it would shift eastward. (However, there may be instances when the visible hot spot shifts eastward and the mid-IR hot spot shifts westward, occurring just after clouds begin to form on the eastern dayside but have yet to be transported to the western dayside after their journey to the nightside.) Furthermore, the westward shift of the “hot spot” in the visible band and the eastward shift of the “hot spot” in the mid-IR band may occur simultaneously, both corresponding to higher cloud coverage over the western dayside than the eastern dayside. These phenomena may also coincide with an anomaly of nightside brightness temperature in the mid-IR, due to a cloud greenhouse effect over the nightside. Whether this anomaly of nightside mid-IR brightness temperature is positive or negative may mainly depend on whether the nightside cloud temperature is higher or lower than the surface temperature.

The transit depth variations due to varying cloudiness are only marginally observable. The altitude of the cloud tops could extend several times the atmospheric scale height, which is estimated to be on the order of 50 kilometers, assuming an atmosphere dominated by N_2 , CO, or CO_2 . This is comparable to the 1σ observational uncertainty in the planet’s radius, ~ 150 km ([Meier Valdés et al. 2022](#)).

Future multiband observations of 55 Cancri e’s phase curve and secondary eclipse depths will provide valuable opportunities to test the hypotheses presented in this study. Additionally, detecting spectral features of silicate vapor or silicate clouds ([Wakeford & Sing 2015](#); [Gao et al. 2020](#); [Burningham et al. 2021](#); [Grant et al. 2023](#)) will further support this hypothesis.

5. CONCLUSION

This study proposes that extreme weather indicated by observations of the ultra-hot rocky exoplanet 55 Cnc e correspond to limit-cycle oscillations in surface temperature and cloudiness. In the limit cycle, high surface temperatures lead to increased silicate vapor supply to the atmosphere. The vapor can condense and form reflective clouds, which cool the surface and throttle the vapor supply needed to sustain cloudiness. A lag between peak surface temperature and accelerated cloud formation—likely due to lagged vapor transport from the substellar magma ocean to the cloud formation zone—allows limit-cycle oscillations. We find that these oscillations can occur across a wide range of atmospheric and magma ocean conditions.

While there are important limitations of this model (that could be addressed in future by more sophisticated GCMs that incorporate silicate clouds), a simple model of the proposed oscillations is sufficient to explain the observed variability in mid-IR brightness: the highest mid-IR brightness corresponds to the strongest surface emission at the highest surface temperature after extended cloud-free periods, while the lowest mid-IR brightness corresponds to cloud-top or surface emission temperature that occurs at the maximum cloudiness and the lowest surface temperature. The proposed oscillations can also lead to the observed variability in the brightness in the visible band: the highest visible brightness corresponds to the strongest starlight reflection by cloud at the maximum cloudiness, while the lowest visible brightness corresponds to the weakest surface emission from the coolest surface right after cloud dispersion. Our model predicts out-of-phase oscillations in secondary eclipse depths in different spectral bands, as found by recent observations. The different horizontal distribution of cloud during different stages of the oscillation may also explain the observed “hot spot” shifts in the visible and mid-IR bands and can lead to correlated “hot spot” shifts and

brightness temperature anomalies on both the dayside and nightside, which could be confirmed by future multiband observations of 55 Cancri e’s phase curve and secondary eclipse depths.

Acknowledgments. The project was made possible by the summer school *Rosbypalooza: Clouds and convection in diverse climates*. Rosbypalooza is funded by the University Corporation for Atmospheric Research (UCAR), National Science Foundation (NSF) and the Department of the Geophysical Sciences, and Graduate Council (GC) at the University of Chicago.

Code and data availability. Model and data visualization code available at <https://github.com/kaitlyn-loftus/lava-limits>

Software. DifferentialEquations.jl (Rackauckas & Nie 2017; Widmann & Rackauckas 2022) Makie.jl (Danisch & Krumbiegel 2021)

APPENDIX

A. ESTIMATING MODEL PARAMETERS

The model parameters Π_1 , Π_2 , and Π_3 are defined as

$$\Pi_1 = \frac{3k_1 M_v}{2g M_{\text{air}} \rho_c r_c}, \quad (\text{A1})$$

$$\Pi_2 = \frac{2k_2 g^2 M_{\text{air}} \rho_c r_c^2 d}{9R^* T_0 \eta}, \quad (\text{A2})$$

and

$$\Pi_3 = \frac{c_p \rho_m H_{\text{mix}}}{d}. \quad (\text{A3})$$

Table 2 lists estimates for the individual parameters that constitute the three model parameters. The upper and lower bounds for the three model parameters in Table 1 are calculated based on the values and bounds for individual parameters in Table 2.

REFERENCES

- Bourrier, V., Ehrenreich, D., Des Etangs, A. L., et al. 2018a, *Astronomy & Astrophysics*, 615, A117, doi: [10.1051/0004-6361/201832700](https://doi.org/10.1051/0004-6361/201832700)
- Bourrier, V., Dumusque, X., Dorn, C., et al. 2018b, *Astronomy & Astrophysics*, 619, A1, doi: [10.1051/0004-6361/201833154](https://doi.org/10.1051/0004-6361/201833154)
- Burningham, B., Faherty, J. K., Gonzales, E. C., et al. 2021, *MNRAS*, 506, 1944, doi: [10.1093/mnras/stab1361](https://doi.org/10.1093/mnras/stab1361)
- Colby, F. P. 1984, *Monthly Weather Review*, 112, 2239, doi: [10.1175/1520-0493\(1984\)112<2239:CIAAPO>2.0.CO;2](https://doi.org/10.1175/1520-0493(1984)112<2239:CIAAPO>2.0.CO;2)
- Crane Company. 1988, *Flow of Fluids through Valves, Fittings and Pipe* (Crane Company)
- Danisch, S., & Krumbiegel, J. 2021, *Journal of Open Source Software*, 6, 3349, doi: [10.21105/joss.03349](https://doi.org/10.21105/joss.03349)
- Dawson, R. I., & Fabrycky, D. C. 2010, *The Astrophysical Journal*, 722, 937, doi: [10.1088/0004-637X/722/1/937](https://doi.org/10.1088/0004-637X/722/1/937)
- Demory, B.-O., Gillon, M., Madhusudhan, N., & Queloz, D. 2016a, *Monthly Notices of the Royal Astronomical Society*, 455, 2018, doi: [10.1093/mnras/stv2239](https://doi.org/10.1093/mnras/stv2239)
- Demory, B.-O., Gillon, M., Seager, S., et al. 2012, *The Astrophysical Journal Letters*, 751, L28, doi: [10.1088/2041-8205/751/2/L28](https://doi.org/10.1088/2041-8205/751/2/L28)
- Demory, B.-O., Gillon, M., Deming, D., et al. 2011, *Astronomy & Astrophysics*, 533, A114, doi: [10.1051/0004-6361/201117178](https://doi.org/10.1051/0004-6361/201117178)
- Demory, B.-O., Gillon, M., De Wit, J., et al. 2016b, *Nature*, 532, 207, doi: [10.1038/nature17169](https://doi.org/10.1038/nature17169)
- Demory, B.-O., Sulis, S., Valdés, E. M., et al. 2023, *Astronomy and Astrophysics*, 669, A64, doi: [10.1051/0004-6361/202244894](https://doi.org/10.1051/0004-6361/202244894)
- Fan, B., Habib, N., Spaulding-Astudillo, F., Kite, E. S., & Li, C. 2022, in *AGU Fall Meeting Abstracts*, Vol. 2022, P42A-03

Table 2. Estimated bounds for individual model parameters that constitute Π_1 , Π_2 , and Π_3

parameter	physical meaning	value or bounds	note
R^*	universal gas constant	$8.3144 \text{ J mol}^{-1} \text{ K}^{-1}$	
g	gravitational acceleration	22 m s^{-2}	From Bourrier et al. (2018b)
M_v	molar mass of the cloud-forming vapor	44 g mol^{-1}	For SiO
M_{air}	mean molar mass of the background atmosphere	$28\text{--}44 \text{ g mol}^{-1}$	Considering CO, N ₂ , and CO ₂ , supported by Hu et al. (2024)
ρ_c	density of cloud particles	$2100\text{--}3600 \text{ kg m}^{-3}$	Lower bound: for SiO, upper bound: for Mg ₂ SiO ₄
r_c	mean radius of cloud particles	$0.2\text{--}30 \text{ }\mu\text{m}$	From Powell et al. (2018)
T_0	representative atmospheric temperature	$675\text{--}3000 \text{ K}$	Lower bound: stratospheric skin temperature based on the lowest observed nightside brightness temperature, upper bound: the highest surface temperature
η	dynamic viscosity of the background atmosphere	$4.6 \times 10^{-5}\text{--}8.0 \times 10^{-5} \text{ kg m}^{-1} \text{ s}^{-1}$	Lower bound: for N ₂ or CO at 1500 K, upper bound: for CO ₂ at 3000 K, from Weast et al. (1986) ; Crane Company (1988)
c_p	specific heat capacity of magma	$1090\text{--}2360 \text{ J kg}^{-1} \text{ K}^{-1}$	Lower bound: for FeO melt, upper bound: for MgO melt, from Lange & Navrotsky (1992)
ρ_m	density of magma	$2180\text{--}2800 \text{ kg m}^{-3}$	Lower bound: for rhyolitic magma, upper bound: for basaltic magma
H_{mix}	thickness of the mixed layer of the surface magma ocean	$1\text{--}1000 \text{ m}$	Upper bound referenced from Lai et al. (2024b,a)
d	time delay between high surface temperature and accelerated cloud formation	$1 \text{ hour to } 10 \text{ days}$	Lower bound: surface-to-cloud vertical transport timescale, upper bound: horizontal transport timescale to encircle the planet
k_1	scale factor accounting for uncertainties in the scaling for the increase rate of cloud optical depth	$0.001\text{--}1$	Lower bound: limited supersaturation, particle nucleation barriers, subsaturated near-surface atmosphere, mixing with ambient air
k_2	scale factor accounting for uncertainties in the scaling for the residence time of cloud	$0.1\text{--}100$	Lower bound: non-spherical particles (Ohno et al. 2020), cloud depth uncertainty, upper bound: particle growth, cloud depth uncertainty (Rossow 1978)

Fegley, B., & Cameron, A. 1987, *Earth and Planetary Science Letters*, 82, 207, doi: [10.1016/0012-821X\(87\)90196-8](#)

Fischer, D. A., Marcy, G. W., Butler, R. P., et al. 2008, *The Astrophysical Journal*, 675, 790, doi: [10.1086/525512](#)

Folsom, C., Fionnagáin, D. Ó., Fossati, L., et al. 2020, *Astronomy & Astrophysics*, 633, A48, doi: [10.1051/0004-6361/201937186](#)

Gao, P., Thorngren, D. P., Lee, E. K., et al. 2020, *Nature Astronomy*, 4, 951, doi: [10.1038/s41550-020-1114-3](#)

Grant, D., Lewis, N. K., Wakeford, H. R., et al. 2023, *ApJL*, 956, L32, doi: [10.3847/2041-8213/acfc3b10.3847/2041-8213/acfdab](#)

Hammond, M., & Pierrehumbert, R. T. 2017, *The Astrophysical Journal*, 849, 152, doi: [10.3847/1538-4357/aa9328](#)

He, C., Radke, M., Moran, S. E., et al. 2024, *Nature Astronomy*, 8, 182, doi: [10.1038/s41550-023-02140-4](#)

Helling, C. 2019, *Annual Review of Earth and Planetary Sciences*, 47, 583, doi: [10.1146/annurev-earth-053018-060401](#)

Heng, K. 2023, *The Astrophysical Journal Letters*, 956, L20, doi: [10.3847/2041-8213/acfe05](#)

Heng, K. 2024, *ApJL*, 971, L52, doi: [10.3847/2041-8213/ad6863](#)

Hu, R., Bello-Arufe, A., Zhang, M., et al. 2024, *Nature*, 1, doi: [AsecondaryatmosphereontherockyExoplanet55Cancerie](#)

- Katz, R. F., Spiegelman, M., & Langmuir, C. H. 2003, *Geochemistry, Geophysics, Geosystems*, 4, 1, doi: [10.1029/2002GC000433](https://doi.org/10.1029/2002GC000433)
- Kennedy, C. A., & Carpenter, M. H. 2003, *Applied numerical mathematics*, 44, 139, doi: [10.1016/S0168-9274\(02\)00138-1](https://doi.org/10.1016/S0168-9274(02)00138-1)
- Kite, E., Kreidberg, L., Schaefer, L., Caracas, R., & Hirschmann, M. 2021, *Eos, Transactions American Geophysical Union*, 102, doi: [10.1029/2021EO159473](https://doi.org/10.1029/2021EO159473)
- Kite, E. S., Fegley Jr, B., Schaefer, L., & Gaidos, E. 2016, *The Astrophysical Journal*, 828, 80, doi: [10.3847/0004-637X/828/2/80](https://doi.org/10.3847/0004-637X/828/2/80)
- Lai, Y., Kang, W., & Yang, J. 2024a, arXiv preprint arXiv:2408.09985, doi: [10.48550/arXiv.2408.09985](https://doi.org/10.48550/arXiv.2408.09985)
- Lai, Y., Yang, J., & Kang, W. 2024b, arXiv preprint arXiv:2408.09986, doi: [10.48550/arXiv.2408.09986](https://doi.org/10.48550/arXiv.2408.09986)
- Lange, R. A., & Navrotsky, A. 1992, *Contributions to Mineralogy and Petrology*, 110, 311, doi: [10.1007/BF00310746](https://doi.org/10.1007/BF00310746)
- Lee, E. K., Blecic, J., & Helling, C. 2018, *Astronomy & Astrophysics*, 614, A126, doi: [10.1051/0004-6361/201731977](https://doi.org/10.1051/0004-6361/201731977)
- Mahapatra, G., Helling, C., & Miguel, Y. 2017, *Monthly Notices of the Royal Astronomical Society*, 472, 447, doi: [10.1093/mnras/stx1666](https://doi.org/10.1093/mnras/stx1666)
- McKay, M. D., Beckman, R. J., & Conover, W. J. 2000, *Technometrics*, 42, 55, doi: [10.2307/1268522](https://doi.org/10.2307/1268522)
- Meier Valdés, E., Morris, B. M., Wells, R. D., Schanche, N., & Demory, B.-O. 2022, *Astronomy & Astrophysics*, 663, A95, doi: [10.1051/0004-6361/202243768](https://doi.org/10.1051/0004-6361/202243768)
- Meier Valdés, E., Morris, B., Demory, B.-O., et al. 2023, *Astronomy & Astrophysics*, 677, A112, doi: [10.1051/0004-6361/202346050](https://doi.org/10.1051/0004-6361/202346050)
- Mercier, S. J., Dang, L., Gass, A., Cowan, N. B., & Bell, T. J. 2022, *The Astronomical Journal*, 164, 204, doi: [10.3847/1538-3881/ac8f22](https://doi.org/10.3847/1538-3881/ac8f22)
- Morris, B., Delrez, L., Brandeker, A., et al. 2021, *Astronomy & Astrophysics*, 653, A173, doi: [10.1051/0004-6361/202140892](https://doi.org/10.1051/0004-6361/202140892)
- Nguyen, T. G., Cowan, N. B., Banerjee, A., & Moores, J. E. 2020, *Monthly Notices of the Royal Astronomical Society*, 499, 4605, doi: [10.1093/mnras/staa2487](https://doi.org/10.1093/mnras/staa2487)
- Ohno, K., Okuzumi, S., & Tazaki, R. 2020, *The Astrophysical Journal*, 891, 131, doi: [10.3847/1538-4357/ab44bd](https://doi.org/10.3847/1538-4357/ab44bd)
- Patel, J., Brandeker, A., Kitzmann, D., et al. 2024, arXiv preprint arXiv:2407.12898, doi: [10.48550/arXiv.2407.12898](https://doi.org/10.48550/arXiv.2407.12898)
- Pierrehumbert, R. T. 2010, *Principles of planetary climate* (Cambridge University Press), doi: [10.1017/CBO9780511780783](https://doi.org/10.1017/CBO9780511780783)
- Powell, D., Zhang, X., Gao, P., & Parmentier, V. 2018, *The Astrophysical Journal*, doi: [10.3847/1538-4357/aac215](https://doi.org/10.3847/1538-4357/aac215)
- Rackauckas, C., & Nie, Q. 2017, *Journal of open research software*, 5, 15, doi: [10.5334/jors.151](https://doi.org/10.5334/jors.151)
- Rappaport, S., Levine, A., Chiang, E., et al. 2012, *ApJ*, 752, 1, doi: [10.1088/0004-637X/752/1/1](https://doi.org/10.1088/0004-637X/752/1/1)
- Rossow, W. B. 1978, *icarus*, 36, 1, doi: [10.1016/0019-1035\(78\)90072-6](https://doi.org/10.1016/0019-1035(78)90072-6)
- Schaefer, L., & Fegley, B. 2004, *Icarus*, 169, 216, doi: [10.1016/j.icarus.2003.08.023](https://doi.org/10.1016/j.icarus.2003.08.023)
- . 2009, *The Astrophysical Journal*, 703, L113, doi: [10.1088/0004-637X/703/2/L113](https://doi.org/10.1088/0004-637X/703/2/L113)
- Tamburo, P., Mandell, A., Deming, D., & Garhart, E. 2018, *The Astronomical Journal*, 155, 221, doi: [10.3847/1538-3881/aabd84](https://doi.org/10.3847/1538-3881/aabd84)
- Tan, X., & Showman, A. P. 2019, *The Astrophysical Journal*, 874, 111, doi: [10.3847/1538-4357/ab0c07](https://doi.org/10.3847/1538-4357/ab0c07)
- . 2021a, *Monthly Notices of the Royal Astronomical Society*, 502, 678, doi: [10.1093/mnras/stab060](https://doi.org/10.1093/mnras/stab060)
- . 2021b, *Monthly Notices of the Royal Astronomical Society*, 502, 2198, doi: [10.1093/mnras/stab097](https://doi.org/10.1093/mnras/stab097)
- von Braun, K., Boyajian Tabettha, S., ten Brummelaar, T. A., et al. 2011, *The Astrophysical Journal*, 740, 1, doi: [10.1088/0004-637X/740/1/49](https://doi.org/10.1088/0004-637X/740/1/49)
- Wakeford, H. R., & Sing, D. K. 2015, *Astronomy and Astrophysics*, 573, 1, doi: [10.1051/0004-6361/201424207](https://doi.org/10.1051/0004-6361/201424207)
- Weast, R. C., Astle, M. J., & Beyer, W. H. 1986, *CRC Handbook of Chemistry and Physics* (CRC Press)
- Widmann, D., & Rackauckas, C. 2022, arXiv preprint arXiv:2208.12879, doi: [10.48550/arXiv.2208.12879](https://doi.org/10.48550/arXiv.2208.12879)
- Winn, J. N., Matthews, J. M., Dawson, R. I., et al. 2011, *The Astrophysical Journal Letters*, 737, L18, doi: [10.1088/2041-8205/737/1/L18](https://doi.org/10.1088/2041-8205/737/1/L18)
- Zeidler, S., Posch, T., Mutschke, H., Richter, H., & Wehrhan, O. 2011, *Astronomy & Astrophysics*, 526, A68, doi: [10.1051/0004-6361/201015219](https://doi.org/10.1051/0004-6361/201015219)